

The SAIL dataset of marine atmospheric electric field observations over the Atlantic Ocean

Susana Barbosa¹, Nuno Dias^{1,2}, Carlos Almeida^{1,2}, Guilherme Amaral^{1,2}, António Ferreira^{1,2}, António Camilo³, and Eduardo Silva^{1,2}

¹INESC TEC - INESC Technology & Science, Porto, Portugal

²ISEP, Instituto Superior de Engenharia do Porto, Porto

³CINAV. Marinha, Lisboa, Portugal

Correspondence: Susana Barbosa (susana.a.barbosa@inesctec.pt)

Abstract.

A unique dataset of marine atmospheric electric field observations over the Atlantic Ocean is described. The data are relevant not only for atmospheric electricity studies, but more generally for studies of the Earth's atmosphere and climate variability, as well as space-earth interactions studies. In addition to the atmospheric electric field data, the dataset includes simultaneous measurements of other atmospheric variables, including gamma radiation, visibility, and solar radiation. These ancillary observations not only support interpretation and understanding of the atmospheric electric field data, but are also of interest in themselves. The entire framework from data collection to final derived datasets has been ~~dully~~ duly documented to ensure traceability and reproducibility of the whole data curation chain. All the data, from raw measurements to final datasets, are preserved in data repositories with a corresponding assigned DOI. Final datasets are available from the Figshare repository (https://figshare.com/projects/SAIL_Data/178500) and computational notebooks containing the code used at every step of the data curation chain are available from the Zenodo repository (<https://zenodo.org/communities/sail>).

1 Introduction

The atmospheric electric field is an ever-present feature of the Earth's atmosphere, ~~originated from the approximately 1,000 thunderstorms active at any given time on Earth (Rycroft et al., 2000). The strong air currents inside a thunderstorm cloud and the vertical movement of water and ice particles causes the separation of electric charges and an electric current to flow up to the ionosphere.~~ Since the surface of the Earth and the ionosphere are good conductors, while the atmosphere is a reasonably good electrical insulator, an electric current ~~flows through the majority of the Earth's atmosphere in the "fair weather" region remote from thunderstorms, and through the Earth's crust~~ flowing through the the Earth's atmosphere connects the Earth's surface to the ionosphere, constituting Earth's global electrical circuit (e.g Markson (2007); Rycroft et al. (2008); Williams (2009)). The small density current flowing between the ionosphere and the Earth's surface is only of the order of a picoampere per square meter (10^{-12} Am^{-2}) but it is able to produce a vertical electric field between 100 and 300 Vm^{-1} near ground level (e.g. Burns et al. (2012)).

The global atmospheric electric field exhibits diurnal variability driven by the ~~daily variation of thunderstorm activity throughout the Earth~~variation of global thunderstorm activity, influenced by the tropical distribution of land masses, above which thunderstorms preferentially form ~~at the end of the day (Wilson, 1921)~~late in the day (local time). Non-lightning-producing storms (referred as electrified shower clouds) are also an important contribution to the global electric circuit, as proposed initially by (Wilson, 1921). Both thunderstorms and electrified shower clouds contribute to global electric circuit through the descent of negative charge (Mach et al., 2010; Liu et al., 2010; Mach et al., 2011; Williams and Mareev, 2014).

The global nature of the Earth's electric field, and its diurnal variability, were confirmed by data collected in a series of campaigns aboard the *Carnegie* vessel between 1915 and 1929, showing that the electric field exhibits a diurnal variation, reaching its highest values at 19:00 UTC, regardless of the location on the globe (Parkinson, 1931; Torreson, 1946). This diurnal variation ~~became~~came to be known as the "Carnegie curve", and it is used to this day as the reference for the diurnal variation of the global atmospheric electric field (~~Harrison, 2013, 2020~~)(Markson, 2007; Harrison, 2013, 2020).

This diurnal feature of the global atmospheric electric field is hard to observe in non-marine measurements of the electric field, as it is usually hidden by local sources of variability including aerosols and particulates, ambient radioactivity, and anthropogenic influences such as power lines, electrical infrastructure and communication systems. Marine measurements of the atmospheric electric field are therefore very relevant for several atmospheric studies, but rare. ~~And in a Buoy measurements of the atmospheric electric field are becoming available (Wilson and Cummins, 2021), with the advantage of detailed monitoring for prolonged periods of time at a specific location, though lacking the spatial distribution enabled by ship-based observations.~~

In a climate change context~~the need of such observations-~~the need for such observations of the atmospheric electric field over the ocean is even more compelling, as the electrical conductivity of the ocean air is clearly linked to global atmospheric pollution and aerosol content (Price, 1993; Rycroft et al., 2000; Harrison, 2004). Measurements from the research vessel *Oceanographer* in 1967 indicated values of atmospheric electrical conductivity consistent with the original Carnegie observations in the remote South Pacific, but a decrease over the Atlantic of at least 20%, which was attributed to an increase in North hemisphere aerosol pollution (Cobb and Wells, 1970). Here we present a unique dataset of atmospheric electric field measurements performed over the Atlantic Ocean in the scope of the SAIL (Space-Atmosphere-ocean Interactions in the marine boundary Layer) project (Barbosa et al., 2023c). Section 2 gives an overview of the monitoring campaign and methodology for collecting the data, section 3 describes the dataset and applied quality assurance procedures, and concluding remarks are provided in section 5.

2 Monitoring campaign

The SAIL monitoring campaign started on January 5th 2020 aboard the Portuguese navy ship *NRP Sagres* (Figure 1) for an initially planned circum-navigation expedition of 371 days. However, the voyage was interrupted due to the covid pandemic, and the campaign was thus restricted to the Atlantic Ocean. Figure 2 depicts the ship's trajectory during the SAIL campaign.

55 After a short stop at Cape Town for provisions, the ship departed the same day back to Portugal, having arrived [to Lisboa in Lisbon](#) on May 10th, after a required technical stop for repairs at Cabo Verde.



Figure 1. [Photo of the NRP Sagres ship in full sail; the inset shows the location on the mast of the gamma radiation sensor \(black cylinder, left\) and of the primary electric field CS-110 sensor \(right\).](#)

The monitoring system of the SAIL campaign is described in detail in Barbosa et al. (2022). In brief, the atmospheric electric field and ancillary variables are measured on the mizzen mast of the *NRP Sagres* ship ([see Figure 1](#)) and transmitted to a dedicated on-board computer. Every measurement is tagged with a timestamp with microsecond precision based on the system clock in coordinated universal time (UTC). The system clock is corrected by a PPS (Pulse Per Second) signal available from a Global Navigation Satellite System (GNSS) receiver.

The atmospheric electric field is measured near the top of the ship's mast, at about 20 meters height, with an automatic electric field meter sensor CS-110 (Campbell Scientific, UK) measuring the vertical component of the electric field by means of [a rotating of an oscillating](#) grounded shutter. A secondary measurement is performed at the same mast but closer to the ship deck, at [an a](#) height of around 5 meters, using an identical instrument. Ancillary atmospheric variables are measured close to the main electric field sensor, at the 20 meters height, and include gamma radiation, visibility, and short-wave solar radiation. Gamma radiation resulting from natural radioactivity, including the radioactive decay of radon gas progeny, and from the interaction of cosmic rays and atmospheric gas molecules, is a direct source of atmospheric ions. Ions influence cloud and aerosol processes (Harrison and Carslaw, 2003) and changes in ion concentration and/or ion mobility impact the local atmospheric electric field by changing atmospheric conductivity (Harrison and Tammet, 2008). Visibility and solar radiation are used to assess atmospheric conditions, as weather conditions causing changes in charge distribution or ion mobility influence the local atmospheric field (e.g. Bennett and Harrison (2007)). [Atmospheric conductivity decreases with increased aerosol concentration \(e.g. Kamsali et al. \(2009\)\), which in turn decreases visibility, as higher aerosol loads scatter and absorb more light. Therefore the presence of aerosol implies both the reduction of the air's electrical conductivity and the visual range \(Brazenor and Harrison, 2005; Harrison, 2012\).](#)

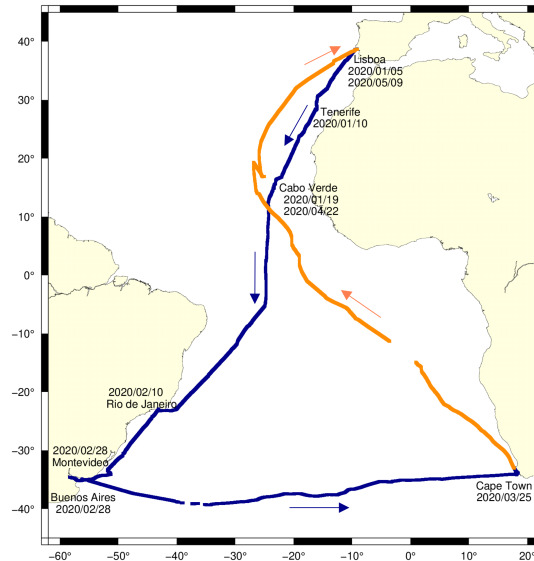


Figure 2. Trajectory of the *NRP Sagres* ship from January to May 2020; blanks correspond to periods with no data.

Gamma radiation is measured with a $76 \times 76 \text{ mm}^2$ NaI(Tl) cylindrical scintillator (Scionix, the Netherlands) equipped with an electronic total count single channel analyzer measuring total counts of gamma radiation in the 475 keV to 3 MeV energy range (Zafrir et al., 2011), which is optimal for the detection of radon progeny (Zafrir et al., 2011). Possible sources of the measured gamma radiation include gamma rays from the radioactive decay of potassium-40 in seawater and from gamma-emitting radionuclides in the uranium and thorium series, typically present in suspended sediments at the ocean surface and attached to atmospheric aerosols. Cosmic radiation contributions are expected to be comparably much smaller since the secondary cosmic radiation reaching the earth's surface is composed by only about 2% of gamma radiation (Wissmann et al., 2007). The scintillator is encased in a water-proof container protecting it from the harsh marine conditions and installed next to the electric field instrument (starboard side), in an upright position and pointing upwards, in order to have the field of view of the instrument towards the atmosphere above, rather than encompassing the ocean surface and the ship itself. Visibility is measured at the port side with a visibility sensor SWS050 (Biral, UK) providing meteorological optical range measurements in the range from 10 m to 40 km. Short-wave solar radiation is measured next to the electric field sensor using incoming (Apogee, SP-510)

and outgoing (Apogee, SP-610) solar radiation sensors. Local meteorological information (rain, atmospheric pressure, temperature, and wind) is manually recorded by the ship's crew every 1 hour as part of the navy's operations routine (meteorological information is not recorded when the ship is ~~not navigating in port~~).

During the 126-days of the SAIL campaign, all measurements were performed continuously at a rate of 1Hz, except for visibility with measurements every 1-minute. Overall data completion is > 95%. Data loss due to malfunction of the monitoring system occurred on 8th and 9th March (during the trip from Buenos Aires to Cape Town) and then from 4 to 6 April (in the leg from Cape Town to Lisboa), due to issues on the onboard computer and storage systems. The ~~voids missing segments~~ in the ship's trajectory represented in Figure 2 correspond to these data gaps. The data management strategy for all the data collected in the scope of the SAIL campaign is detailed in the SAIL data management plan (Barbosa and Karimova, 2021).

3 Data and quality assurance

All the data from the SAIL campaign are preserved in order to foster ~~its~~their reuse in different scientific domains and to enable initially unforeseen uses of the data. All data handling processes are fully documented to ensure traceability and reproducibility.

The raw campaign data (Barbosa et al., 2021) are only available upon request due to its large size (around 700 GB). This dataset of raw measurements includes the data obtained directly from the ship on-board system (designated as ship data), the data (designated as sensor data) obtained from the ship data by correcting logging errors (Amaral and Dias, 2021) and the data (designated as geosensor data) obtained from the sensor data by adding two additional columns corresponding to latitude and longitude based on the GNSS data from the campaign (Ferreira, 2021)~~);~~. The logging errors are caused by non-deterministic communication failures between the instrument and the main onboard computer, as well as occasional power shortages, which result in parsing errors due to incomplete lines and non-standard characters in the output files. Such errors are corrected automatically by in-house developed software that checks the correct number of fields in each line and and removes the line if it does not match the expected count. (Amaral and Dias, 2021).

~~Data~~ Except for the meteorological observations, all data were collected continuously during the SAIL campaign, thus including both measurements performed over the ocean ~~when the ship was sailing,~~ as well as coastal measurements ~~performed taken~~ when the ship was docked ~~during the different stops along its in port~~ during its various stops along the journey (see Figure 2). To facilitate the usage of the data for studies requiring ocean-only observations (e.g. Barbosa et al. (2023b)), a flag denoting fully-ocean days ~~is,~~ when the ship is away from the coast, is added to the final datasets (Figure 3).

Pre-processed data (Barbosa et al., 2023a) are produced from the raw data by implementing quality-control and pre-processing procedures. These procedures and the resulting quality-assured derived datasets are described in section 3.1 for the atmospheric electric field data, and in section 3.2 for the ancillary data.

3.1 Atmospheric electric field

Measurements of the atmospheric electric field are performed with no site-specific corrections. The default value of ~~the sensor~~ (0.1 provided by the CS-110 manufacturer for the site calibration factor, C_{site} , of a sensor with the shutter at 2 meter height) is

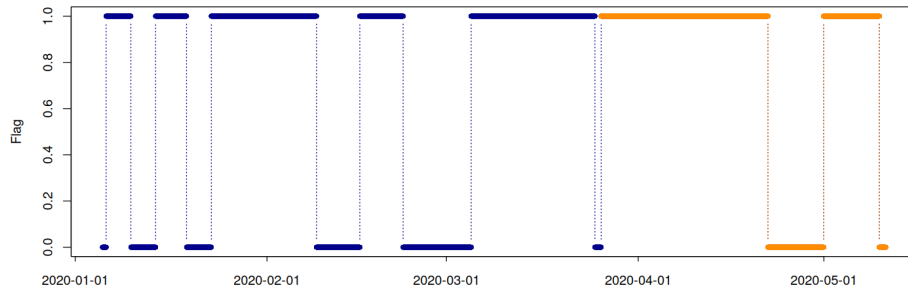


Figure 3. Flag distinguishing fully ocean (=1) and fully or partially land (=0) days for the measurements taken between January 5th and May 9th 2020. The same colours as in Figure 2 are used for the first leg of the ship trajectory (blue) and for the returning leg (orange).

120 used, m above flat ground (Campbell Scientific, Inc., 2023), is used both for the primary instrument and the secondary (lower) one, designated as E1 and E2, respectively. The behaviour of the two instruments is addressed in section 3.1.1.

The raw atmospheric electric field data are first pre-processed for basic quality-control (section 3.1.2). Corrections are applied at a subsequent stage, and are fully documented, in order to be able to trace back all the steps to reproduce and/or to further modify the data processing (section 3.1.3). Selection of fair weather atmospheric electric field data is described in
125 section 3.1.4.

3.1.1 Zero-field measurements

The two electric field instruments were factory-calibrated before the SAIL campaign, and further evaluated after the campaign in terms of zero-field measurements, by using a zero field cover plate attached to the instrument's shutter in its typical downward-facing orientation, enabling to ground any electric field that would be measured by the instrument, and thus assess
130 its potential contamination. The data were collected on land, at the same height of about 2m, over three consecutive days (June 3 to 5, 2022). Figure 4 summarises the zero-field electric field measurements and Figure 5 the corresponding leakage current measurements. These results indicate that the primary electric field sensor has a smaller error and lower leakage current than the secondary sensor, but both sensors perform well, the difference to zero being below 4 V/m and leakage currents below 0.025 nA.

135 3.1.2 Atmospheric electric field data pre-processing

Pre-processing of the raw atmospheric electric field data is documented in Barbosa (2023c), and includes:

- checking the instrument status code; if different than 1 (indicating good instrument health) the corresponding measurement is set as missing (flagged as NA);
 - changing the sign of the atmospheric electric field measurements to comply with the sign convention denoting the potential gradient as positive under undisturbed atmospheric electrical conditions (e.g. Harrison and Nicoll (2018)) since the electric field is downward-directed in fair weather conditions;
- 140

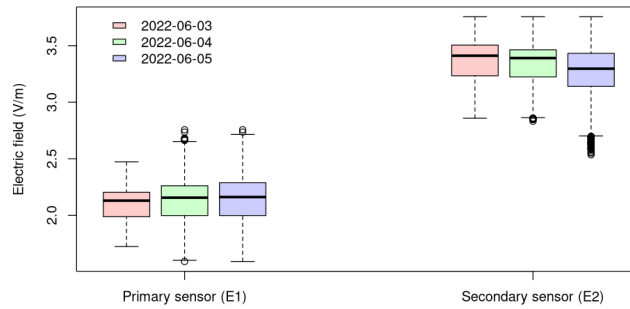


Figure 4. Zero-field Boxplots of zero-field electric field measurements. The lower limit of each box corresponds to the 1st quartile of the values, the upper limit to the 3rd quartile, and the horizontal line inside each box represents the median of the data. The vertical whiskers extend to 1.5 times the interquartile range (3rd quartile minus 1st quartile), and values outside that interval are represented as circles.

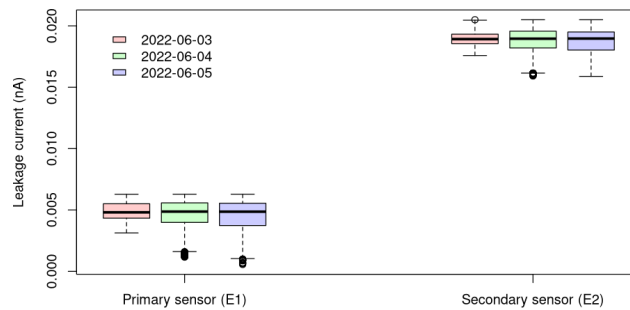


Figure 5. Zero-field Boxplots of zero-field leakage current measurements. Same conventions as for Figure 4.

- averaging 1-second electric field measurements into 1-minute values;
 - averaging geographical coordinates (taking into account angularity) to 1-minute averaged values;
 - computing the standard deviation every 1-minute from the 1-second measurements;
- 145 – checking the record continuity and inserting a flag (NA) for missing times in order to ensure a continuous time series of atmospheric electric field observations.

The pre-processed dataset obtained by applying [these procedures](#) to the raw data ~~these procedures~~ (but before application of the corrections that will be described in section 3.1.3) is available from the INESC TEC data repository (Barbosa et al., 2023a).

Figure 6 presents examples of 1-minute pre-processed electric field observations from the two sensors for days with contrast-
 150 ing weather conditions. These examples emphasise the consistency of the temporal variability of the electric field measurements from the two sensors, on one hand, and on the other hand the large difference in the corresponding values of the atmospheric electric field, with values from the secondary instrument ([Figure 6b](#)) substantially lower and less variable than the ones of the primary instrument ([Figure 6a](#)). These differences are not explainable by differences in the performance of the two instruments (see section 3.1.1) nor by differences in the height of the sensors, as these would not explain the reduced variability of

155 the secondary electric field measurements. Plausibly the differences between primary and secondary electric field observations result from the location of the secondary sensor and consequent field distortion effects. While the primary sensor, near the top of the mast, has relatively unimpeded surroundings, the secondary (lower) sensor is adjacent to several structures of the ship, likely distorting the local electric field. Despite this difficulty the secondary electric field measurements, at the lower height, are kept in the dataset, but their use and interpretation should be cautious, particularly in terms of absolute values.

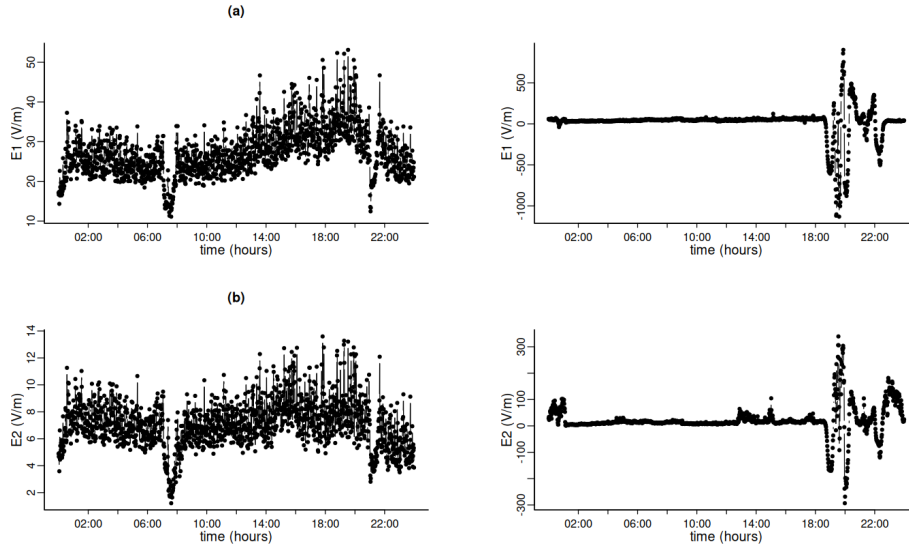


Figure 6. Examples of pre-processed electric field observations for a clear day (on February 2nd, left) and for a rainy day (on January 28th, right), from the primary (higher) instrument (top) and the secondary (lower) instrument (bottom).

160 3.1.3 Atmospheric electric field data corrections

Height-correction for primary electric field measurements

The atmospheric electric field measurements taken on the ship depend on the location of the electric field sensors and are influenced by the ship's geometry. Although the site-related field distortions do not influence relative variations of the atmospheric electric field, they impact absolute values. Quantification of site specific influences is a challenging task. A first attempt to address the difference between measurements due to the location of the sensor on the top mast relative to on-shore measurements is presented in section 3.1.3(a). The differences between the primary electric field sensor, located at the top of the mast, and the secondary sensor, located further down the mast, are addressed in section 3.1.3(b).

165

(a) Correction of primary electric field measurements

The influence of the height at which the primary atmospheric electric field measurements are performed is assessed by considering simultaneous observations of the atmospheric electric field conducted at the height of about 20 meters near the top of the

170

mast (using instrument E1) and at sea level (standard 2 meters height from the ground), with the secondary instrument (E2) placed on shore when the ship was docked at the Lisbon Naval Base (Figure 7). Due to logistic and operational constraints, the measurements were performed for a short period of about 2 hours on June 16th 2020, under fair weather conditions. These simultaneous measurements are presented in Figure 8. The pier measurements exhibit several spikes, which are absent in the mast measurements, likely resulting from human activity at the pier disturbing the electric field measurements. The temporal variability of the two measurements is consistent, with a Pearson's linear correlation coefficient of 0.848, but there is a clear bias between the mast and the pier measurements, the mast measurements being significantly lower (averaging 68 V/m) than the pier measurements (which average 119 V/m). The bias is estimated by means of a linear model, represented in Figure 9. The (positive) correlation between the two measurements is statistically significant ([0.84, 0.85] is the 95% confidence interval) and the fitted linear model has a slope equal to 1.76 (± 0.013), explaining 72% of the variance. The linear model's intercept is zero (statistically not significant). These estimates are used for height correction of the primary measurements of the atmospheric electric field on the mast, by multiplying all the mast observations by 1.76: $E1_{h_corr} = E1 \times 1.76$ (V/m).

Bias correction for (b) Correction of secondary electric field measurements

Figure 10 summarises the height-corrected primary electric field observations and the secondary electric field measurements in terms of its daily median values (Figure 10, right) and in terms of daily median differences $E1_{h_corr} - E2$ (Figure 10, left). The differences are in general positive (primary measurements larger than secondary electric field measurements), averaging 56 V/m. This bias estimate is used to correct secondary electric field observations: $E2_{corr} = E2 + 56$ (V/m).

The datasets of height-corrected primary electric field observations and bias-corrected secondary electric field observations are available from the Figshare repository (Barbosa et al., 2024b). The datasets include the time stamp (in the format yyyy-mm-dd HH:MM:SS), the 1-minute averaged potential gradient in V/m after applying the corrections described above, the corresponding standard deviation in V/m, longitude, latitude, and the flag signalling whether it's a fully ocean day (=1) or a fully or partially land day (=0).

3.1.4 Atmospheric electric field data selection

A dataset of selected atmospheric electric field observations is derived from the dataset of primary corrected electric field observations by applying the following data-driven criteria:

- Non-negative Potential Gradient values (corresponding to 98.6% of the observations);
- Observations flagged as a fully-ocean day (see Figure 3) which correspond to 71.9 % of the observations.

In addition to these criteria, the following fair weather criteria (Harrison and Nicoll, 2018) are applied based on the available ancillary and meteorological information (see section 3.2):

- Dry day, according to manual precipitation records (corresponding to 85.8% of the days);
- Clear sky (meteorological optical range $\geq 30,000$ meters), a condition fulfilled by 60.1 % of the observations.



Figure 7. Photo showing the instruments used for the simultaneous measurements of the atmospheric electric field at the mast and on shore.

The application of these criteria results in retaining 35.6 % of the corrected primary electric field observations. The resulting dataset of these fair weather marine observations of the atmospheric electric field is available from the Figshare repository (Barbosa et al., 2024c).

205 Figure 11 shows the hourly boxplots for the selected fair weather electric field observations -The displaying the median value (horizontal solid line) and the 1st and 3rd quartiles of the observations (lower and upper vertical limits of the box, respectively). The hourly values were computed by averaging the 1-minute electric field observations for each preceding 59 minutes. The Sagres data display the typical Carnegie curve shape, with minimum around 04:00 UTC and maximum around 19:00 UTC, but the amplitude of the curve represented by hourly median values is smaller, of only about 18 V/m, is substantially smaller,
210 corresponding to 30% of the amplitude of the Carnegie curve.

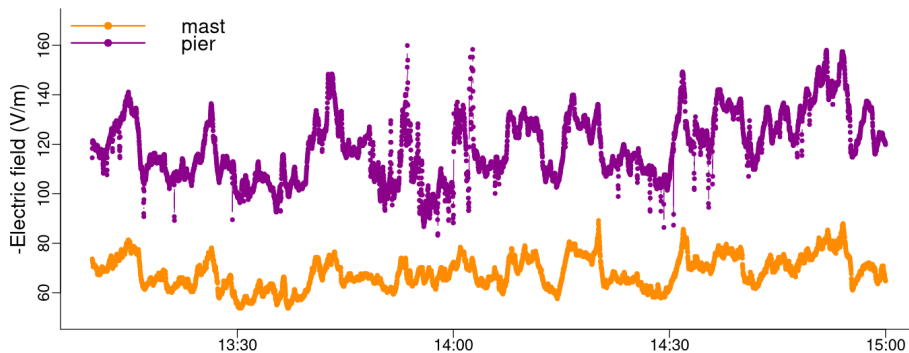


Figure 8. Time series of simultaneous atmospheric electric field measurements every 1-second performed at the mast of the ship (at a height of about 20 meters) and at the pier [in Lisbon Naval Base](#) (at the standard height of 2 meters) [under fair weather conditions in 2020-06-16](#).

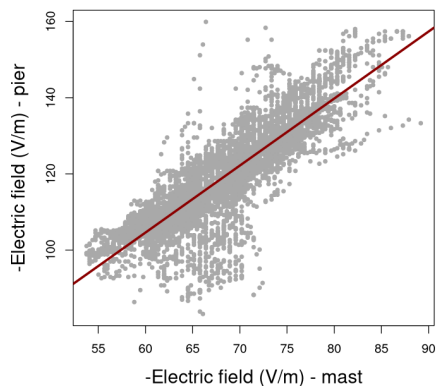


Figure 9. Scatterplot and fitted linear model for the observation represented in Figure 8.

3.2 Ancillary observations

3.2.1 Gamma radiation

Pre-processed gamma radiation data are obtained from the raw data by aggregating [1-second-counts-to-\(adding\) the gamma radiation counts measured every second into](#) 1-minute values, calculating average geographical coordinates every 1-minute, and
 215 by checking data continuity and flagging missing measurements, which correspond to 4.4% of the time series values. Further quality-control is performed by inspecting the pre-processed 1-minute data, and identifying anomalous values, typically sharp spikes (lasting less than 3 minutes), and anomalously low values before/after a data gap (associated with recovery of the instrument after power failure). These outliers (1.2% of the time series values) are set as missing, as exemplified in Figure 12. The jupyter notebook [\(Granger and Pérez, 2021\)](#) implementing these pre-processing and quality-control steps is preserved

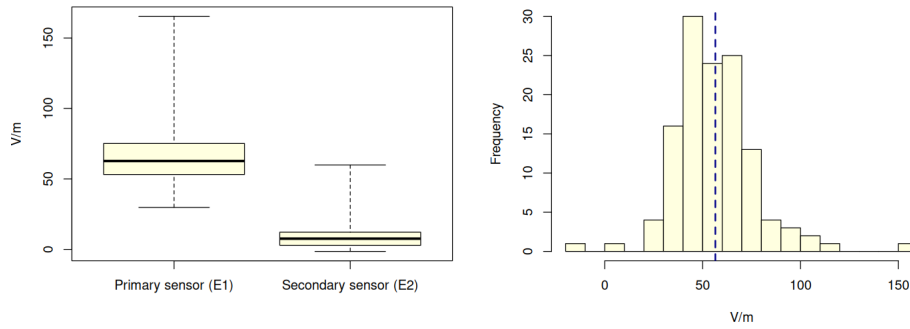


Figure 10. Daily median values of height-corrected primary electric field observations and secondary electric field measurements (left) and corresponding daily median differences $E1_{h_corr} - E2$ (right), the dashed vertical line representing the average of the differences.

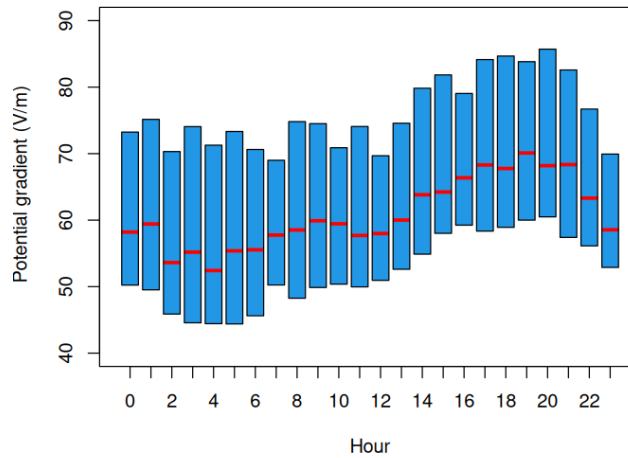


Figure 11. Hourly boxplots (1st to 3rd quartile) of SAIL fair weather atmospheric electric field observations. The horizontal red line represents the hourly median value of the potential gradient.

220 in [Zenodo the Zenodo repository](#) (Barbosa (2025c)). The resulting dataset of quality-assured gamma radiation observations is available from Figshare (Barbosa et al., 2025a).

3.2.2 Visibility

Pre-processed data are obtained by extracting meteorological optical range measurements from the raw visibility data and then checking temporal continuity and inserting a flag (NA) for missing observations, in order to produce a continuous time series
 225 (Barbosa, 2024). The quality-assured time series of meteorological optical range observations is available from the Figshare repository (Barbosa et al., 2024a).

The meteorological optical range measured by the visibility sensor reflects the transparency of the atmosphere, and is an useful parameter to assess local atmospheric conditions. As an example, Figure 13 displays the visibility data for a clear day

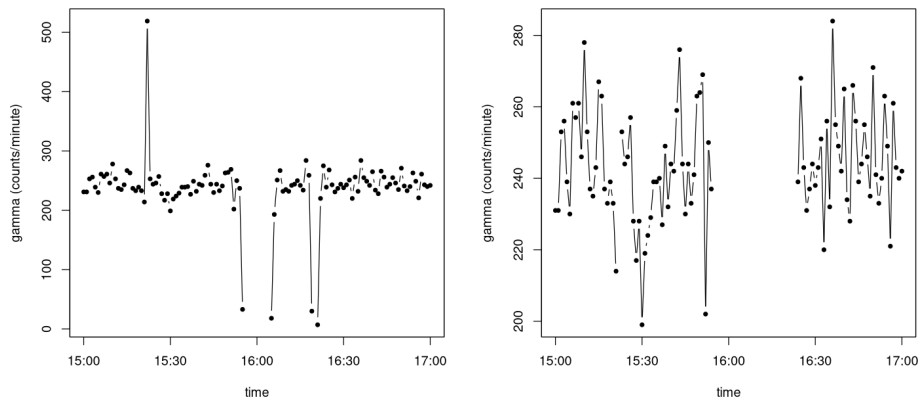


Figure 12. Example (16th January 2020) of pre-processing of 1-minute gamma radiation observations: spikes and anomalously low values before/after a data gap (left) are set as missing (right).

and for a rainy day. In the first case visibility values are consistently high-high and at the upper limit of the instrument's range, except for cloudy conditions reducing visibility around 08:00, while in the latter case visibility values are low, with lowest observations around 17:00 and 19:00, associated with rain episodes.

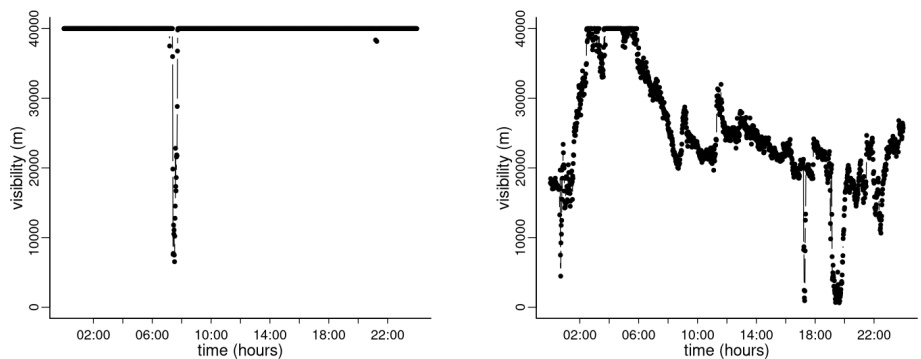


Figure 13. Example of visibility observations for a clear day (on February 2nd, left) and for a rainy day (on January 28th, right).

3.2.3 Solar radiation

Raw solar radiation data every 1-second are pre-processed to produce 1-minute averaged incoming and outgoing short-wave solar radiation. Inspection of the data for quality-control reveals the existence of non-valid negative values of solar radiation. These negative (and small magnitude) values of solar radiation are replaced by zero. Inspection of the incoming solar radiation data for each hour of the day reveals a few small values during night hours, which are set as zero. A much larger number of non-zero night values is found in the case of outgoing radiation - likely reflecting the effect of the ship's own illumination - and these values are set as missing. The jupyter notebooks implementing these quality-control procedures are preserved in

the Zenodo repository (Barbosa, 2025b). The resulting quality-assured datasets of incoming and outgoing short-wave solar radiation are available from the Figshare repository (Barbosa et al., 2025b).

Figure 14 displays an example of the daily variability of 1-minute incoming solar radiation observations for the same days as in Figure 13. For the sunny day the diurnal pattern is more regular and incoming solar radiation values are higher. It must be noted that although the solar radiation sensors were installed high on the mast, some partial shading and/or enhanced reflection by the ship's sails cannot be discarded.

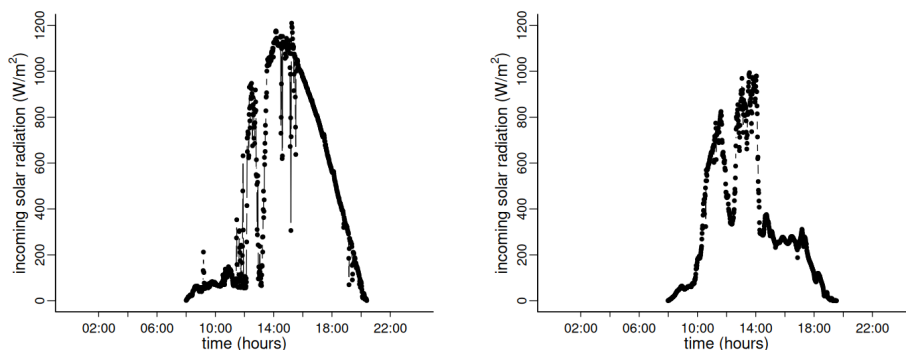


Figure 14. Example of incoming short-wave solar radiation observations for a clear day (on February 2nd, left) and for a rainy day (on January 28th, right).

245 3.2.4 Meteorological information

Local meteorological information is collected every hour by meteorological observers of the ship's crew (Table 1). The raw data (Camilo, 2021) were corrected by homogenising non-standard missing values flags and by removing headers and formatting features in order to enable further automatic processing. The resulting corrected data (Barbosa, 2023b) are subject to further quality-control procedures specific to each meteorological parameter, as detailed in the jupyter notebook made available in
250 [Zenodo](#) [the Zenodo repository](#) (Barbosa, 2023a). These include, in addition to removal of obvious outliers, the translation of visibility classes from Portuguese to English based on WMO-No. 471 (WMO, 2018), and the homogenisation and translation of qualitative precipitation information. The resulting quality-assured dataset of meteorological observations is available from the Figshare repository (Barbosa and Camilo, 2023).

Table 1. Meteorological data over the Atlantic Ocean collected onboard the NRP Sagres ship during the SAIL campaign.

Datafile column	Meteorological variable	Unit / format
1	Date	yyyy-mm-dd
2	Time	HH:MM, local time
3	Latitude	DD° M.M
4	Latitude	suffix (N or S)
5	Longitude	DDD° M.M
6	Longitude	suffix (E or W)
7	QNH (Query Nautical Height)	mbar
8	Temperature - dry bulb	°C
9	Temperature - wet bulb	°C
10	Dew point	°C
11	Relative humidity	%
12	Water temperature - bucket	°C
13	Water temperature - hull	°C
14	True wind direction	°
15	True wind speed	knots
16	True wind force	beaufort scale
17	Wave direction	compass half-wind
18	Wave height	m
19	Visibility	qualitative code ¹
20	Cloud cover	oktas
21	Precipitation	qualitative code ¹

¹ excellent, very good, good, moderate, poor

² moderate, light, drizzle, drizzle moderate, drizzle light

4 Code and data availability

255 All the code and data is publicly available. The project SAIL community on Zenodo (<https://zenodo.org/communities/sail/>) contains the technical documents related to the SAIL data, and the computational (jupyter) notebooks used at the different stages of data processing (Table 2). Raw data (Barbosa et al. (2021), DOI: 10.25747/b2ff-kg31) and pre-processed data (Barbosa et al. (2023a), DOI: 10.25747/58P6-6B76) are available from INESC TEC RDM repository. Final datasets (Table 3) are available from the Figshare repository, under the SAIL data project (https://figshare.com/projects/SAIL_Data/178500).

Table 2. [Code \(Jupyter notebook\) available on the project SAIL community on Zenodo \(https://zenodo.org/communities/sail/\)](https://zenodo.org/communities/sail/).

<u>Title</u>	<u>DOI</u>	<u>Reference</u>
Pre-processing and quality-control of of electric field data	10.5281/zenodo.10276613	Barbosa, 2023c
Pre-processing and quality-control of gamma radiation data	10.5281/zenodo.14803667	Barbosa, 2025c
Pre-processing of visibility data	10.5281/zenodo.11621789	Barbosa, 2024
Pre-processing and quality-control of solar radiation data	10.5281/zenodo.14720715	Barbosa, 2025b
Pre-processing of meteorological data	10.5281/zenodo.10150266	Barbosa, 2023a
Computational notebook for the figures in this paper	10.5281/zenodo.14833426	Barbosa, 2025a

Table 3. [Datasets available on the SAIL data project on Figshare \(https://figshare.com/projects/SAIL_Data/178500\)](https://figshare.com/projects/SAIL_Data/178500).

<u>Title</u>	<u>DOI</u>	<u>Reference</u>
Atmospheric electric field data	10.6084/m9.figshare.19692391.v1	Barbosa et al., 2024b
Fair weather atmospheric electric field data	10.6084/m9.figshare.26022001.v1	Barbosa et al., 2024c
Gamma radiation data	10.6084/m9.figshare.20393931.v4	Barbosa et al., 2025a
Visibility data	10.6084/m9.figshare.19692394.v3	Barbosa et al., 2024a
Solar radiation data	10.6084/m9.figshare.24614754.v2	Barbosa et al., 2025b
Meteorological data	10.6084/m9.figshare.24613869.v1	Barbosa and Camilo, 2023

260 5 Conclusions

The SAIL dataset of marine atmospheric electric field observations over the Atlantic Ocean is a unique dataset, relevant not only for atmospheric electricity studies, but more generally for studies of the Earth’s atmosphere and climate variability, as well as space-earth interactions studies.

265 In addition to the atmospheric electric field measurements, the data presented here ~~includes~~ include simultaneous measurements of other atmospheric variables, including gamma radiation, visibility, and solar radiation. These ancillary data not only support interpretation and understanding of the atmospheric electric field observations, but are of interest in themselves (e.g. Barbosa et al. (2023b)), as data seldom measured over the ocean, and even more rarely at the spatial and temporal resolutions achieved in the SAIL campaign.

270 The measurement of the atmospheric electric field on a tall ship has several challenging aspects, including the variable site geometry, particularly related to the changing configuration of the sails, and field distorting effects due to the ship’s structures. Corrections have been provided according to the best available information, but further simultaneous measurements on the ship mast and on shore, away from the ship’s (and other structures) influence, are clearly desirable. Another possibility to increase confidence on the correction of the atmospheric electric field measurements would be the development of an electrostatic model of the ship’s geometry enabling to simulate deviations in the electric field due to local geometric and conductive influences.

275 Finding the correct reduction factor to adjust the ship observations for the variations introduced by the ship itself was already challenging during the Carnegie cruises (Hewlett, 1914; Torreson, 1946), and continues to be so in modern-day measurements. The absolute values provided for the mentioned limitations can still influence absolute values of the atmospheric electric field need therefore to be taken with caution. Enhanced confidence is ensured by relative atmospheric electric field values.

The entire framework from data collection to final derived datasets has been ~~dully~~ duly documented in order to foster
280 reproducibility of the whole data curation chain, and enable alternative data processing strategies and different corrections to be seamlessly implemented.

A follow-up monitoring of the atmospheric electric field aboard the NRP Sagres ship is currently ongoing, and corresponding datasets will be updated in a future effort.

~~Datasets available on the SAIL data project on Figshare (https://figshare.com/projects/SAIL_Data/178500), Title DOI Reference
285 Atmospheric electric field data 10.6084/m9.figshare.19692391.v1 Barbosa et al., 2024b Fair weather atmospheric electric field data 10.6084/m9.figshare.26022001.v1 Barbosa et al., 2024c Gamma radiation data 10.6084/m9.figshare.20393931.v3 Barbosa et al., 2025 Visibility data 10.6084/m9.figshare.19692394.v3 Barbosa et al., 2024a Solar radiation data 10.6084/m9.figshare.24614754.v1 Barbosa et al., 2025b Meteorological data 10.6084/m9.figshare.24613869.v1 Barbosa and Camilo, 2023~~

Author contributions. SB: conceptualization, data curation, formal analysis, writing - original draft; ND, GA, AF: set-up of monitoring
290 system, data collection; data curation; CA: set-up of monitoring system, data collection; AC, ES: resources, supervision.

Competing interests. The authors declare absence of competing interests.

Acknowledgements. The support provided by the NRP Sagres's crew and the Portuguese Navy is gratefully acknowledged. Project SAIL received funding from the Portuguese Ministry of Environment and Energy Transition through Fundo Ambiental protocol no 9/2020 and by the Portuguese ~~Foundation for Science and Technology (FCT) LA~~ funding agency, FCT - Fundação para a Ciência e a Tecnologia, within
295 project UIDB/P50014/0063/2020. DOI 10.54499/UIDB/50014/2020 <https://doi.org/10.54499/uidb/50014/2020>.

References

- Amaral, G. and Dias, N.: SAIL campaign - Technical report on Sensor Data correction, <https://doi.org/10.5281/zenodo.4518865>, 2021.
- Barbosa, S.: SAIL Jupyter Notebooks - Pre-processing of meteorological data from the SAIL project, <https://doi.org/10.5281/zenodo.10150266>, 2023a.
- 300 Barbosa, S.: Sagres ship corrected meteorological data 2020 [dataset], <https://doi.org/10.25747/FYKZ-9H72>, 2023b.
- Barbosa, S.: SAIL Jupyter Notebooks - Pre-processing and quality-control of electric field data from the SAIL project, <https://doi.org/10.5281/zenodo.10276613>, 2023c.
- Barbosa, S.: SAIL Jupyter Notebooks - Pre-processing of visibility data from the SAIL project, <https://doi.org/10.5281/zenodo.11621789>, 2024.
- 305 Barbosa, S.: Computational notebook for the paper "The SAIL dataset of marine atmospheric electric field observations over the Atlantic Ocean", <https://doi.org/10.5281/zenodo.14833426>, 2025a.
- Barbosa, S.: SAIL Jupyter Notebooks - Pre-processing and quality-control of solar radiation data from the SAIL project, <https://doi.org/10.5281/zenodo.14720715>, 2025b.
- Barbosa, S.: SAIL Jupyter Notebooks - Pre-processing and quality-control of gamma radiation data from the SAIL project, <https://doi.org/10.5281/zenodo.14803667>, 2025c.
- 310 Barbosa, S. and Camilo, A.: SAIL - Meteorological data, <https://doi.org/10.6084/m9.figshare.24613869.v1>, 2023.
- Barbosa, S. and Karimova, Y.: SAIL Data Management Plan, <https://doi.org/10.5281/zenodo.4286209>, 2021.
- Barbosa, S., Almeida, C., Amaral, G., Dias, N., Ferreira, A., Almeida, J. M., Camilo, A., David, G., Karimova, Y., Lima, L., Martins, A., Oliveira, R., Ribeiro, C., Silva, I., and Silva, E.: Raw data collected onboard the Sagres ship during the SAIL project campaign [dataset], <https://doi.org/10.25747/b2ff-kg31>, 2021.
- 315 Barbosa, S., Dias, N., Almeida, C., Amaral, G., Ferreira, A., Lima, L., Silva, I., Martins, A., Almeida, J., Camilo, M., and Silva, E.: An holistic monitoring system for measurement of the atmospheric electric field over the ocean - the SAIL campaign, in: OCEANS 2022 - Chennai, p. 1–5, <https://doi.org/10.1109/OCEANSCennai45887.2022.9775273>, 2022.
- Barbosa, S., Almeida, C., Amaral, G., Dias, N., and Ferreira, A.: Pre-processed atmospheric data from the SAIL campaign onboard the Sagres ship [Data set], <https://doi.org/10.25747/58P6-6B76>, 2023a.
- 320 Barbosa, S., Dias, N., Almeida, C., Silva, G., Ferreira, A., Camilo, A., and Silva, E.: Precipitation-Driven Gamma Radiation Enhancement Over the Atlantic Ocean, *J Geophys Rese-Atmos*, 128, e2022JD037 570, <https://doi.org/10.1029/2022JD037570>, 2023b.
- Barbosa, S., Dias, N., Amaral, G., Ferreira, A., Almeida, C., and Maurício Camilo, A.: SAILing to research Earth's climate , *INESC TEC Science & Society*, 1, <https://science-society.inesctec.pt/index.php/inesctecesociedade/article/view/114>, 2023c.
- 325 Barbosa, S., Almeida, C., Amaral, G., Dias, N., Ferreira, A., Camilo, A., and Silva, E.: SAIL - Visibility data [dataset], <https://doi.org/10.6084/m9.figshare.19692394.v3>, 2024a.
- Barbosa, S., Almeida, C., Amaral, G., Dias, N., Ferreira, A., Camilo, A., and Silva, E.: SAIL - Atmospheric electric field data, <https://doi.org/10.6084/m9.figshare.19692391.v1>, 2024b.
- Barbosa, S., Almeida, C., Amaral, G., Dias, N., Ferreira, A., Camilo, A., and Silva, E.: SAIL - Fair weather atmospheric electric field data, <https://doi.org/10.6084/m9.figshare.26022001.v1>, 2024c.
- 330 Barbosa, S., Almeida, C., Amaral, G., Dias, N., Ferreira, A., Camilo, A., and Silva, E.: SAIL - gamma radiation data [dataset], <https://doi.org/10.6084/m9.figshare.20393931.v4>, 2025a.

- Barbosa, S., Almeida, C., Amaral, G., Dias, N., Ferreira, A., Camilo, A., Silva, E., and Coelho, L.: SAIL - Solar radiation data, <https://doi.org/10.6084/m9.figshare.24614754.v2>, 2025b.
- 335 Bennett, A. J. and Harrison, R. G.: Atmospheric electricity in different weather conditions, *Weather*, 62, 277–283, <https://doi.org/10.1002/wea.97>, 2007.
- Brazenor, T. and Harrison, R.: Aerosol modulation of the optical and electrical properties of urban air, *Atmospheric Environment*, 39, 5205–5212, <https://doi.org/https://doi.org/10.1016/j.atmosenv.2005.05.022>, 2005.
- Burns, G., Tinsley, B., Frank-Kamenetsky, A., Troshichev, O., French, W., and Klekociuk, A.: Monthly diurnal global atmospheric circuit estimates derived from Vostok electric field measurements adjusted for local meteorological and solar wind influences, *J Atmos Sci*, 69, 2061–2082, 2012.
- 340 Camilo, A.: Sagres ship meteorological data 2020 [dataset], <https://doi.org/10.25747/rp31-kf14>, 2021.
- Campbell Scientific, Inc.: CS-110 Electric field meter Product Manual, <https://s.campbellsci.com/documents/au/manuals/cs110.pdf>, 2023.
- Cobb, W. E. and Wells, H. J.: The electrical conductivity of oceanic air and its correlation to global atmospheric pollution, *J Atmos Sci*, 27, 814–819, 1970.
- 345 Ferreira, A.: SAIL campaign - Technical report on GNSS Post- processing, <https://doi.org/10.5281/zenodo.4447619>, 2021.
- Granger, B. E. and Pérez, F.: Jupyter: Thinking and Storytelling With Code and Data, *Computing in Science & Engineering*, 23, 7–14, <https://doi.org/10.1109/MCSE.2021.3059263>, 2021.
- Harrison, R.: Aerosol-induced correlation between visibility and atmospheric electricity, *Journal of Aerosol Science*, 52, 121–126, <https://doi.org/https://doi.org/10.1016/j.jaerosci.2012.04.011>, 2012.
- 350 Harrison, R. and Nicoll, K.: Fair weather criteria for atmospheric electricity measurements, *J Atmos Solar-Terr Phy*, 179, 239–250, <https://doi.org/10.1016/j.jastp.2018.07.008>, 2018.
- Harrison, R. G.: The global atmospheric electrical circuit and climate, *Surv Geophys*, 25, 441–484, 2004.
- Harrison, R. G.: The carnegie curve, *Surv Geophys*, 34, 209–232, 2013.
- 355 Harrison, R. G.: Behind the curve: a comparison of historical sources for the Carnegie curve of the global atmospheric electric circuit, *Hist Geo- Space Sci*, 11, 207–213, <https://doi.org/10.5194/hgss-11-207-2020>, 2020.
- Harrison, R. G. and Carslaw, K. S.: Ion-aerosol-cloud processes in the lower atmosphere, *Rev Geophys*, 41, <https://doi.org/10.1029/2002RG000114>, 2003.
- Harrison, R. G. and Tammet, H.: Ions in the Terrestrial Atmosphere and Other Solar System Atmospheres, *Space Sci Rev*, 137, 107–118, <https://doi.org/10.1007/s11214-008-9356-x>, 2008.
- 360 Hewlett, C.: The atmospheric-electric observations made on the second cruise of the Carnegie, *Journal of Geophysical Research*, 19, 127–170, <https://doi.org/10.1029/TE019I003P00127>, 1914.
- Kamsali, N., Prasad, B., and Datta, J.: Atmospheric electrical conductivity measurements and modeling for application to air pollution studies, *Advances in Space Research*, 44, 1067–1078, <https://doi.org/10.1016/J.ASR.2009.05.020>, 2009.
- 365 Liu, C., Williams, E., Zipser, E., and Burns, G.: Diurnal Variations of Global Thunderstorms and Electrified Shower Clouds and Their Contribution to the Global Electrical Circuit, *Journal of the Atmospheric Sciences*, 67, 309–323, <https://doi.org/10.1175/2009JAS3248.1>, 2010.
- Mach, D. M., Blakeslee, R. J., Bateman, M. G., and Bailey, J. C.: Comparisons of total currents based on storm location, polarity, and flash rates derived from high-altitude aircraft overflights, *Journal of Geophysical Research: Atmospheres*, 115, 2010.

- 370 Mach, D. M., Blakeslee, R. J., and Bateman, M. G.: Global electric circuit implications of combined aircraft storm electric current measurements and satellite-based diurnal lightning statistics, *Journal of Geophysical Research: Atmospheres*, 116, <https://doi.org/10.1029/2010JD014462>, 2011.
- Markson, R.: The global circuit intensity: Its measurement and variation over the last 50 years, *B A Meteorol Soc*, 88, 223–242, 2007.
- Parkinson, W.: The diurnal variation of the electric potential of the atmosphere over the oceans, *UGGI (Sect. Terr. Magn. Elec.)*, p. 340–341, 375 1931.
- Price, C.: Global surface temperatures and the atmospheric electrical circuit, *Geophys Res Lett*, 20, 1363–1366, 1993.
- Rycroft, M., Israelsson, S., and Price, C.: The global atmospheric electric circuit, solar activity and climate change, *J Atmos Solar-Terr Phy*, 62, 1563–1576, [https://doi.org/10.1016/S1364-6826\(00\)00112-7](https://doi.org/10.1016/S1364-6826(00)00112-7), 2000.
- Rycroft, M. J., Harrison, R. G., Nicoll, K. A., and Mareev, E. A.: An overview of earth's global electric circuit and atmospheric conductivity, 380 *Space Sci Rev*, 137, 83–105, <https://doi.org/10.1007/s11214-008-9368-6>, 2008.
- Torreson, O. W.: Ocean atmospheric-electric results, *Oceanography III: Scientific results of Cruise VII during 1928-1929 under Command of Captain JP Ault*, 1946.
- Williams, E. and Mareev, E.: Recent progress on the global electrical circuit, *Atmospheric Research*, 135-136, 208–227, <https://doi.org/10.1016/j.atmosres.2013.05.015>, 2014.
- 385 Williams, E. R.: The global electrical circuit: A review, *Atmos Res*, 91, 140–152, <https://doi.org/10.1016/j.atmosres.2008.05.018>, 13th International Conference on Atmospheric Electricity ICAE 2007, 2009.
- Wilson, C. T. R.: Investigations on lightning discharges and on the electric field of thunderstorms, *Philosophical Transactions of the Royal Society of London. Series A, Containing Papers of a Mathematical or Physical Character*, 221, 73–115, 1921.
- Wilson, J. G. and Cummins, K. L.: Thunderstorm and fair-weather quasi-static electric fields over land and ocean, *Atmospheric Research*, 390 257, 105 618, <https://doi.org/https://doi.org/10.1016/j.atmosres.2021.105618>, 2021.
- Wissmann, F., Rupp, A., and Stöhlker, U.: Characterization of dose rate instruments for environmental radiation monitoring, *Kerntechnik*, 72, 193–198, 2007.
- WMO: Guide to Marine Meteorological Services (Appendix 2), Tech. rep., 2018.
- Zafir, H., Haquin, G., Malik, U., Barbosa, S., Piatibratova, O., and Steinitz, G.: Gamma versus alpha sensors for Rn-222 long-term monitoring in geological environments, *Radiat Meas*, 46, 611–620, <https://doi.org/10.1016/j.radmeas.2011.04.027>, 2011. 395